Computational Materials Science 247 (2025) 113483

Contents lists available at ScienceDirect

Computational Materials Science

journal homepage: www.elsevier.com/locate/commatsci

Full length article

Impacts of point defects on shallow doping in cubic boron arsenide: A first principles study

Shuxiang Zhou [a,*], Zilong Hua [a], Kaustubh K. Bawane [a], Hao Zhou [b], Tianli Feng [b]

[a] *Idaho National Laboratory, Idaho Falls, ID 83415, USA*
[b] *Department of Mechanical Engineering, University of Utah, Salt Lake City, UT 84112, USA*

ARTICLE INFO

Keywords:
Boron arsenide
Point defect
Doping
Impurity
Density Functional theory

ABSTRACT

Cubic boron arsenide (BAs) stands out as a promising material for advanced electronics, thanks to its exceptional thermal conductivity and ambipolar mobility. However, effective control of p- and n-type doping in BAs poses a significant challenge, mostly as a result of the influence of defects. In the present study, we employed density functional theory (DFT) to explore the impacts of the common point defects and impurities on p-type doping of Be_B and Si_{As}, and on n-type doping of Si_B and Se_{As}. We found that the most favorable point defects formed by C, O, and Si are C_{As}, O_BO_{As}, Si_{As}, $C_{As}Si_B$, and O_BSi_{As}, which have formation energies of less than 1.5 eV. While the O impurity detrimentally affects both p- and n-type dopings, C and Si impurities are harmful for n-type dopings, making n-type doping a potential challenge. Interestingly, the antisite defect pair As_BB_{As} benefits both p- and n-type doping. The doping limitation analysis presented in this study can potentially pave the way for strategic development in the area of BAs-based electronics.

1. Introduction

Over the last decade, cubic boron arsenide (BAs) has attracted an extremely high level of research interest, due to its exceptional thermal conductivity and ambipolar mobility. The thermal conductivity of BAs (i.e., ~1300 W/m K at room temperature, which is only surpassed by diamond for bulk materials) was predicted via theory [1–3], then validated by experiments [4–6]. The simultaneously high room-temperature electron and hole mobilities were also predicted by theory [7] and later confirmed through recent experiments [8,9]. Beyond its remarkable transport properties, BAs is applicable to existing III–V semiconductor technologies [10] and has an electronic structure similar to that of Si, but with a wider band gap [11]. These attributes position BAs as a promising material for advanced electronics and efficient heat management.

One critical need in high-performance electronic applications relates to the development of methodologies for controlling p- and n-type doping to generate the desired ionizable delocalized (shallow) impurity states [12]. To accomplish this, the behaviors of defects such as intrinsic defects and impurities must be comprehensively understood, as they widely existed in experiments [13–15]. Recently, the synthesis of millimeter-sized BAs crystals is achieved via the chemical vapor transport method [15–18], however, a substantial variance is still observed in the measured thermal properties of BAs [5,14,19,20]. Additionally, p-type semiconducting behavior is observed experimentally [17,20,21], indicating the presence of intrinsic defects and/or impurities in BAs samples. For BAs, extensive researches [8,22–26] have been performed on the thermal conductivity reduction caused by intrinsic defects and impurities, however, comparably less emphasis has been placed on comprehending how intrinsic defects and impurities affect electronic properties. Notably, first principles calculations [22,27] were utilized to explore the formation of intrinsic defects, identifying the antisite pair As_BB_{As} as being the most prevalent intrinsic defect type. As the antisite pair As_BB_{As} is usually charge-neutral, it cannot explain the observed p-type semiconducting behavior. Recently, theoretical studies attribute the p-type semiconducting behavior of BAs to impurities such as Si, C, and H [27,28], whereas experiments have validated the presence of Si, C, O, H, Te, and I impurities in BAs [25]. Therefore, impurities may solely induce p-type behavior in BAs and have the potential to influence both p- and n-type doping limitations.

Furthermore, the first principles calculations identified specific dopants (e.g., Be_B and Si_{As} for p-type, and Si_B and Se_{As} for n-type) characterized as shallow dopants [27,28]. A high p-dopability of BAs is also reported [28–31]. However, how various point defects influence the behaviors of shallow dopants has never comprehensively been investigated. For the present work, we conducted a thermodynamic analysis demonstrating the interaction between point defects and shallow dopants, utilizing density functional theory (DFT).

---

* Corresponding author.
E-mail address: shuxiang.zhou@inl.gov (S. Zhou).

https://doi.org/10.1016/j.commatsci.2024.113483
Received 27 June 2024; Received in revised form 15 October 2024; Accepted 25 October 2024

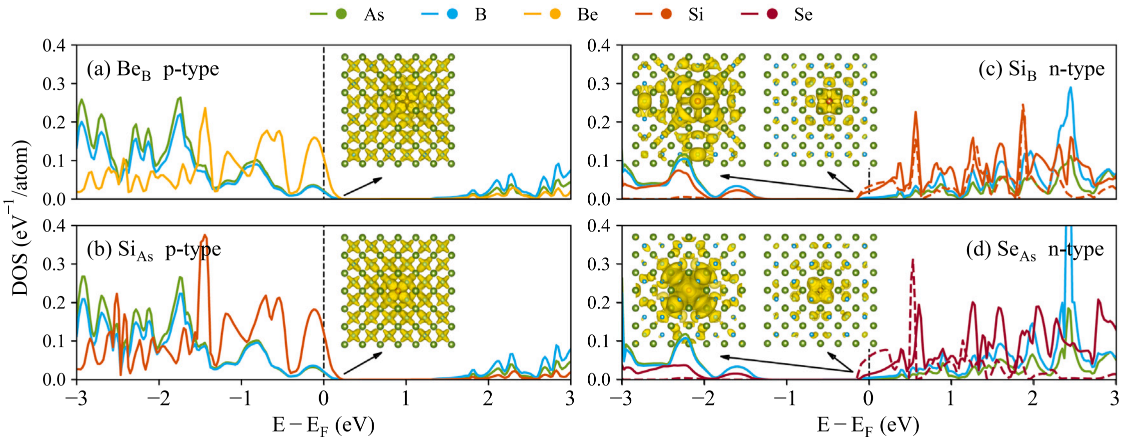

Fig. 1. Calculated electronic DOS of BAs doped by (a) $\mathrm{Be_B}$, (b) $\mathrm{Si_{As}}$, (c) $\mathrm{Si_B}$, and (d) $\mathrm{Se_{As}}$. The solid curves represent the DOS projection on *p* orbitals of each element, while the dashed curves represent the *s* orbital projection. The inset figures are the isosurfaces of charge density near the CBM or VBM (<0.1 eV), depicted at 4×10^{-5} Å^{-3}. The differently colored atoms represent different species.

2. Computational details

In the present work, the DFT calculations were carried out using the projector augmented-wave method [32,33], as implemented in the Vienna ab initio Simulation Package code [34,35]. As the main target of this work is to explore different configurations involving both dopants and point defects, we applied the generalized gradient approximation (GGA) as formulated by Perdew, Burke, and Ernzerhof functional revised for solids (PBEsol) [36] to reduce the computational cost. Besides that, the total charge of the defect systems was kept neutral, following Ref. [12]. For all calculations, spin polarization, a plane-wave cutoff energy of 700 eV, and an energy convergence criterion of 10^{-6} eV were applied. For the defect calculations, a 3 × 3 × 3 supercell of the conventional cubic cell (216 atoms) and a 2 × 2 × 2 Γ-centered k-point mesh were employed, as used in Ref. [12]. The relaxed lattice parameter of the conventional cubic cell of BAs was 4.778 Å, which is fixed in the calculations of defected structures.

Through this work, $\mathcal{X}$ is used to denote the defects in the BAs crystal. According to the discussed dopings, $\mathcal{X}$ is categorized into three subsets, the dopants $\mathcal{D}$, other impurities or intrinsic defects $\mathcal{I}$, and their complex $\mathcal{D}-\mathcal{I}$. Additionally, $\mathrm{Y_{S_Y}}$ is used to represent a single defect, a substitutional Y atom (or V for a vacancy) in the $\mathrm{S_Y}$ site, and $\mathrm{Y_{S_Y}Z_{S_Z}}$ is used to represent a defect pair of coupled $\mathrm{Y_{S_Y}}$ and $\mathrm{Z_{S_Z}}$ single defects. The defect sites, $\mathrm{S_Y}$ and $\mathrm{S_Z}$, can only be B or As in BAs.

The key properties computed are the formation energies, electronic density of states (DOS), and the isosurfaces of charge density. The formation energy values quantified the ease of defect formation, while the isosurfaces of charge density were employed to visualize the spatial localization of impurity states, as an indicator of shallow doping state. The formation energy E_f of defect $\mathcal{X}$ is calculated as:

$$E_f(\mathcal{X}) = E(\mathcal{X}) - E_0 - \sum_i n_i^{\mathcal{X}}(E_i + \mu_i) \tag{1}$$

where E_0 is the total energy of the pristine system, $E(\mathcal{X})$ is the total energy of the defect system, $n_i^{\mathcal{X}}$ is the change in the number of atoms of species i due to defect $\mathcal{X}$ (positive if atoms are added, negative if atoms are removed), E_i is the energy per atom in the elemental phase, and μ_i is the chemical potential of species i. The elemental phases of species B, As, C, O, Si, Be, and Se were considered by using α-B, α-As, graphite, oxygen molecule, Si in the diamond structure, Be in the hexagonal close-packed structure, and α-Se, respectively. Additionally for oxygen molecules, due to the well-known self-interaction error using DFT [37], an energy correction is applied by using the suggested value from the fitted elemental-phase reference energies [4]. For all species i, $\mu_i \le 0$. Furthermore, for all impurity atoms and dopants, μ_i was approximated as zero. The values of μ_B and μ_{As} depend on the growth condition involved: in the As-rich condition, $\mu_{As} = 0$; otherwise, $\mu_B = 0$ in the B-rich condition. Additionally, μ_B and μ_{As} are restricted by the equilibrium condition $\mu_B + \mu_{As} = \Delta H_{BAs}$, where ΔH_{BAs} is the formation enthalpy of BAs. Throughout this work, we use the As-rich condition, following Ref. [22]. Nevertheless, the PBEsol-predicted value of ΔH_{BAs} is merely −0.056 eV, meaning that the differences in μ_B (or μ_{As}) between As- and B-rich conditions only total −0.056 eV, which is trivial. Assuming a defect $\mathcal{I}$ is already present in the system, the formation energy of a dopant $\mathcal{D}$ can be determined using the formula $E_f^{\mathcal{I}}(\mathcal{D}) = E_f(\mathcal{D}-\mathcal{I}) - E_f(\mathcal{I})$ (see Sec. I of SM for more details). Comparing $E_f^{\mathcal{I}}(\mathcal{D})$ against $E_f(\mathcal{D})$ affords insight into whether the defect $\mathcal{I}$ is advantageous for the formation of the dopant $\mathcal{D}$. For DOS, p orbitals of each element were plotted as solid curves throughout this work, and s orbitals were plotted only when it had a higher contribution than p orbitals near the Fermi level E_F, by using dashed curves. The isosurfaces of charge density were visualized using the VESTA package [38], depicted for each band at 4×10^{-5} Å^{-3}, unless for strongly localized bands, which is depicted at 1×10^{-3} Å^{-3} and will be explicitly pointed out.

3. Results

3.1. Shallow dopants

Here we begin by identifying the dopants. Previous studies [27,28] suggest that p-type dopants $\mathrm{Be_B}$ and $\mathrm{Si_{As}}$ and n-type dopants $\mathrm{Se_{As}}$ and $\mathrm{Si_B}$ are shallow dopants with low formation energies. We confirmed that the formation energies of $\mathrm{Be_B}$ (0.15 eV), $\mathrm{Si_{As}}$ (0.42 eV), $\mathrm{Si_B}$ (1.76 eV), and $\mathrm{Se_{As}}$ (1.47 eV) are the lowest among the computed dopants (see Section II of SM for more details). Note that for p-type doping ($\mathrm{Be_B}$ and $\mathrm{Si_{As}}$), the formation energy is substantially lower than that for n-type doping ($\mathrm{Se_{As}}$ and $\mathrm{Si_B}$), thus supporting the notion that p-type doping occurs more readily in BAs than does n-type doping [27,28]. In addition, the DOS and isosurface of charge density were computed for $\mathrm{Be_B}$, $\mathrm{Si_{As}}$, $\mathrm{Si_B}$, and $\mathrm{Se_{As}}$ (see Fig. 1), as well as the electronic band structures (see Section V of SM). For $\mathrm{Be_B}$ and $\mathrm{Si_{As}}$, while the Fermi level E_F slightly shifts into the valence bands, there are three-fold degenerated bands at the valence band maximum (VBM), and their

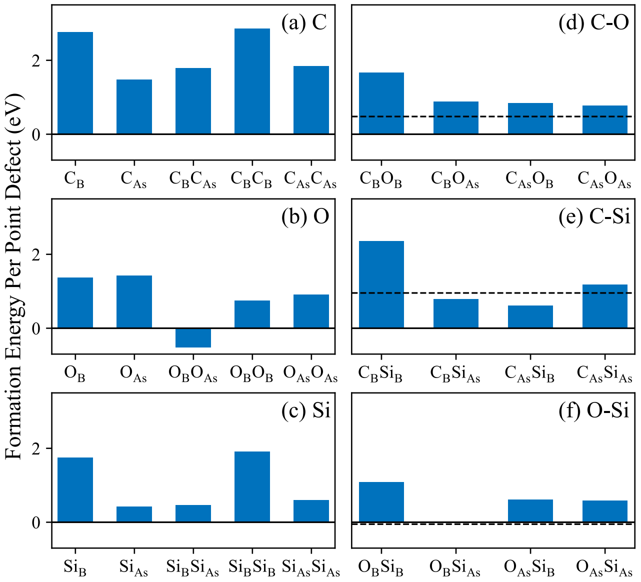

Fig. 2. Calculated formation energy per point defect formed by (a) C, (b) O, (c) Si, (d) C and O, (e) C and Si, and (f) Si and O, in pristine BAs. The dashed lines in (d), (e), and (f) indicate the mean value of the formation energy per point defect of isolated (d) C_{As} and O_BO_{As}, (e) C_{As} and Si_{As}, and (f) O_BO_{As} and Si_{As}, respectively.

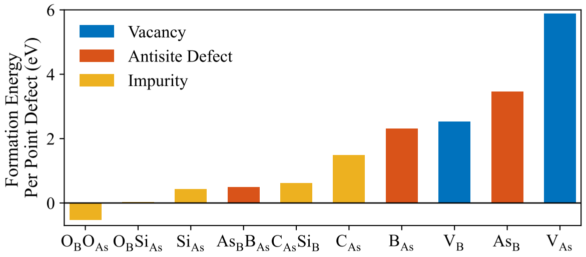

Fig. 3. Calculated formation energy of selected single point defects and point defect pairs. The obtained results are organized in ascending order.

isosurfaces of charge density all exhibit strong spatially delocalized nature from p orbitals, indicating the shallow acceptor nature of Be_B and Si_{As}. For Se_{As} and Si_B, the Fermi level E_F slightly shifts into the conduction bands (see Fig. 1(c) and (d)). Two bands are observed near E_F, and strong localized s-orbital contribution from the impurities, Si and Se, are observed, both from the isosurfaces and DOS. Only one band shows moderately delocalized behavior (left insets), indicating the shallow donor nature of Se_{As} and Si_B. The p orbital DOS of B is at least 60% larger than that of As near E_F, thus the spatial delocalization is mainly contributed by the p orbitals of B. In summary, we use Be_B, Si_{As}, Si_B, and Se_{As} in further investigations regarding the influence of point defects, while DOS and isosurfaces of charge density work as indicators of the shallow state nature.

3.2. Point defects

Given the multitude of configurations involving different species and atom sites for point defects, it is imperative to select the most representative ones. First, we considered C, O, and Si as the impurity elements, due to their high concentration as substitutional impurities, as reported in Ref. [25]. As a reference, the covalent radius, electronegativity, and common charges for defect elements are summarized in Section III of SM. Secondly, we restricted our consideration to single point defects and point defect pairs in the first nearest neighbor. All considered defect structures are presented using Kröger–Vink notation [39] in Section IV of SM. For each situation, we only picked the point defect with the lowest formation energy (see Fig. 2). Panels (a), (b), and (c) reflect situations in which individual C, O, and Si impurities existed, respectively, whereas panels (d), (e), and (f) reflect situations in which combinations of C and O, C and Si, and O and Si impurities coexisted, respectively. Note that, for a direct comparison, the y-axis value is the formation energy per point defect, meaning that the formation energy of defect pairs is divided by two. Per Fig. 2(a)–(c), C_{As}, O_BO_{As}, and Si_{As} are the most favorable point defects when C, O, and Si are the only impurity elements, respectively. In Fig. 2(d), rather than forming defect pairs, C and O impurities are more likely to form isolated C_{As} and O_BO_{As} (indicated by the dashed line). In contrast, C and Si atoms are more likely to form $C_{As}Si_B$, as opposed to isolated C_{As} and Si_{As} (indicated by the dashed line). When O and Si coexist, the formation energy per point defect of O_BSi_{As} is 0.04 eV, and the mean formation energy per point defect of O_BO_{As} and Si_{As} is −0.10 eV (see Fig. 2(f)). Given the small difference (0.14 eV) between these two values, we exceptionally count in O_BSi_{As} into further investigation. To summarize, we selected C_{As}, O_BO_{As}, Si_{As}, $C_{As}Si_B$, and O_BSi_{As} as representative point defects of impurity. Notably, the lowest formation energy is for O_BO_{As} (−0.53 eV), and the possible reason for the negative value is discussed in Section II of SM.

We also examined the intrinsic point defects, including antisite single defects As_B and B_{As}, antisite defect pair As_BB_{As}, and single vacancies V_B and V_{As}. The formation energy per point defect for each of these intrinsic defects is plotted alongside the selected point defects of impurity, moving from the smallest formation energy (left) to the largest (right) (see Fig. 3). Certainly, only the antisite defect pair As_BB_{As} has a formation energy comparable to that of the selected point defects of impurity. Thus, we will discuss a total of six types of point defects, (i.e., the aforementioned five selected types of impurities, plus As_BB_{As}), with the formation energies per point defect all being less than 1.5 eV.

3.3. Effects of point defects on shallow doping

Finally, we discuss the impact of these common point defects (As_BB_{As}, C_{As}, O_BO_{As}, Si_{As}, C_{As}, Si_B, and O_BSi_{As}) on both the formation energy and the electronic characteristics of shallow dopants Be_B, Si_{As}, Si_B, and Se_{As}. Please note that concerning Si_{As} being regarded as a p-type dopant, Si_{As} itself is no longer categorized as a point defect of impurity, while $C_{As}Si_B$ and O_BSi_{As} continue to be considered as impurities due to the presence of C and O. In Section VII of SM, we consider additional point defects As_B, B_{As}, and N_{As}, despite their potential lack of favorability within the BAs system. When different point defects are present, the dopants may occupy various atom sites. For each combination of point defect and dopant, all possible dopant sites within 6 Å of the point defects are computed. Section VI of SM tabulates the detailed calculation results. Here, we only focus on the configuration with the lowest total energy and, consequently, the lowest formation energy.

We start with examining the electronic characteristics via the depiction of DOS and isosurfaces of charge density of Be_B doping (see Fig. 4(a)). As mentioned above, Be_B and Si_{As} feature three-fold degenerated bands at VBM, and the presence of point defects may break the symmetry of the degenerated bands. In this case, only the highest band at VBM is shown as inset figures in Fig. 4(a) and (b), while all bands within 0.1 eV of VBM are provided in enlarged figures in Sec. VIII of SM. Interestingly, the p-type shallow state of Be_B is maintained in the presence of all point defects, except O_BO_{As}, given that the Fermi level

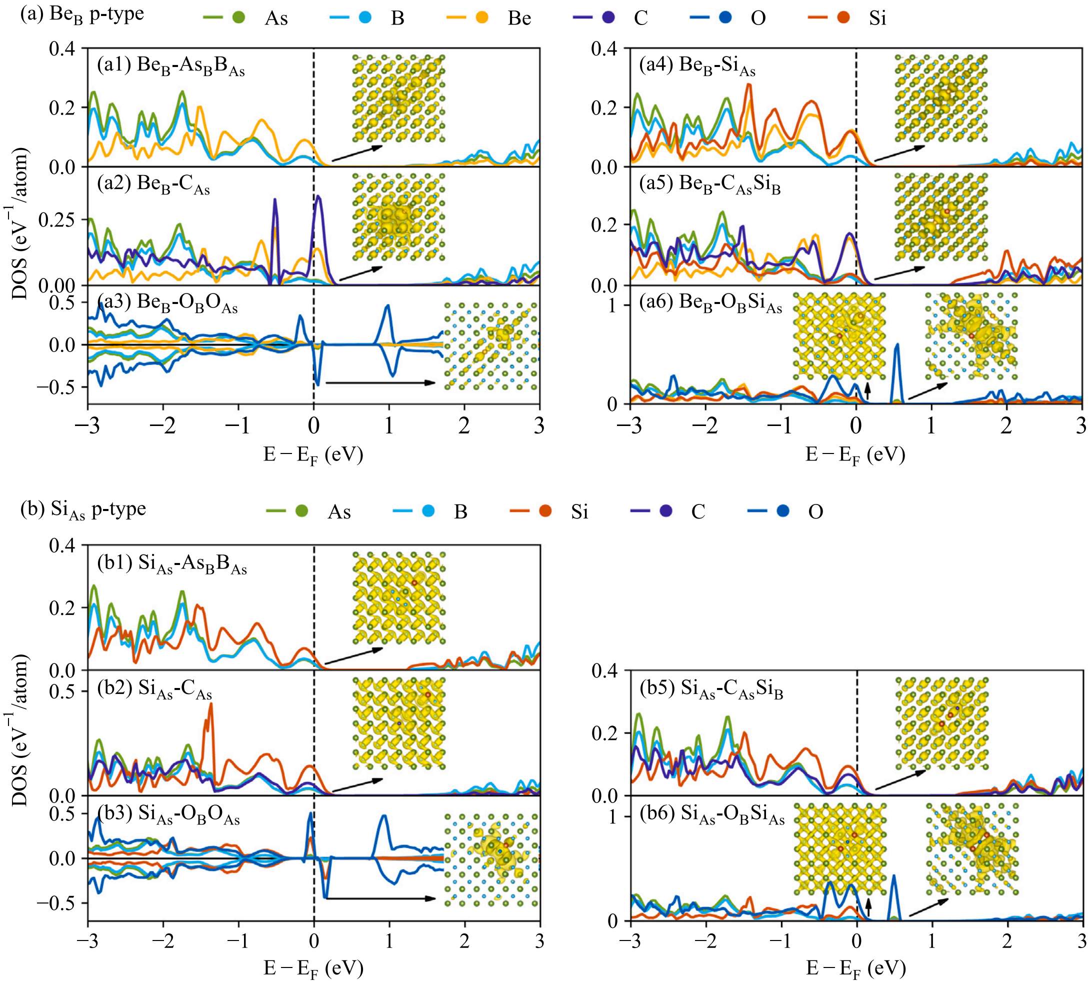

Fig. 4. Calculated electronic DOS of BAs doped by p-type dopants (a) Be_B and (b) Si_{As} in the presence of (1) As_BB_{As}, (2) C_{As}, (3) O_BO_{As}, (4) Si_{As}, (5) $C_{As}Si_B$, or (6) O_BSi_{As} point defects. The solid curves represent the DOS projection on p orbitals of each element. The inset figures show the isosurfaces of charge density near VBM (<0.1 eV) or within the band gap, depicted at 4×10^{-5} Å^{-3} (except for O_BSi_{As}, which is depicted at 1×10^{-3} Å^{-3}). The differently colored atoms represent different species.

E_F is still positioned slightly below VBM, and the isosurfaces of charge density near VBM continue to exhibit spatial delocalization contributed from p orbitals of both B and As. This result is understandable for the charge-neutral defects As_BB_{As} and $C_{As}Si_B$, as well as for the acceptor-like defects C_{As} and Si_{As}, though the acceptor-like defects slightly shift the E_F deeper into the valence band. For the donor-like defects O_BSi_{As}, a localized defect trap state within the band gap. Despite the narrowed band gaps, the p-type shallow state near E_F is still maintained. The only detrimental case is the donor-like defects O_BO_{As}, where a localized defect trap state forms at the top of VBM. For the other p-type dopant Si_{As}, the results are similar to those for Be_B; namely, As_BB_{As}, C_{As}, $C_{As}Si_B$, and O_BSi_{As} all sustain the shallow state (see Fig. 4(b)). The only difference is that O_BO_{As} now forms a localized defect trap state in the middle of the band gap where E_F is positioned, which is still detrimental. Even the top bands of VBM remain the shallow doping nature, Si_{As} have to be doped beyond compensation limits to remedy the move of the Fermi level E_F.

Nevertheless, in the case of n-type dopants Si_B and Se_{As}, the examined point defects exert a more significant influence, owing to the acceptor-like nature of C_{As} and Si_{As} impurities – for which the Fermi level E_F is no longer in the conduction bands – thereby destroying the n-type nature (see Fig. 5(a) and (b)). Additionally, both O_BO_{As} and O_BSi_{As} form localized defect trap states within the band gap where E_F is located. As a result, the charge-neutral defects As_BB_{As} and $C_{As}Si_B$ are the only defects that preserve the n-type shallow state, giving that E_F is marginally above CBM, and one of the bands near CBM exhibits moderate spatial delocalization while the other becomes predominantly localized.

Furthermore, we now provide a synopsis regarding the formation energy of dopants in the presence of point defects. The bars in Fig. 6 illustrate $E_f^{\mathcal{I}}(\mathcal{D})$, the formation energy of the dopants $\mathcal{D}$ in the presence of each point defect $\mathcal{I}$. The dashed black lines denote $E_f(\mathcal{D})$, the formation energy of the dopants without point defects. Green signifies that the delocalized doping state of the original type is preserved, whereas red indicates otherwise. This color is defined by the DOS and isosurface results given in Figs. 4 and 5. Three distinct scenarios are covered: (1) a bar above the dashed line implies that the defect does not couple with the dopant, thus merely impacting the doping; (2) a red bar below the dashed line signifies that a coupled complex of the defect and dopant will likely form, potentially compromising the originally targeted doping state; and (3) a green bar below the dashed

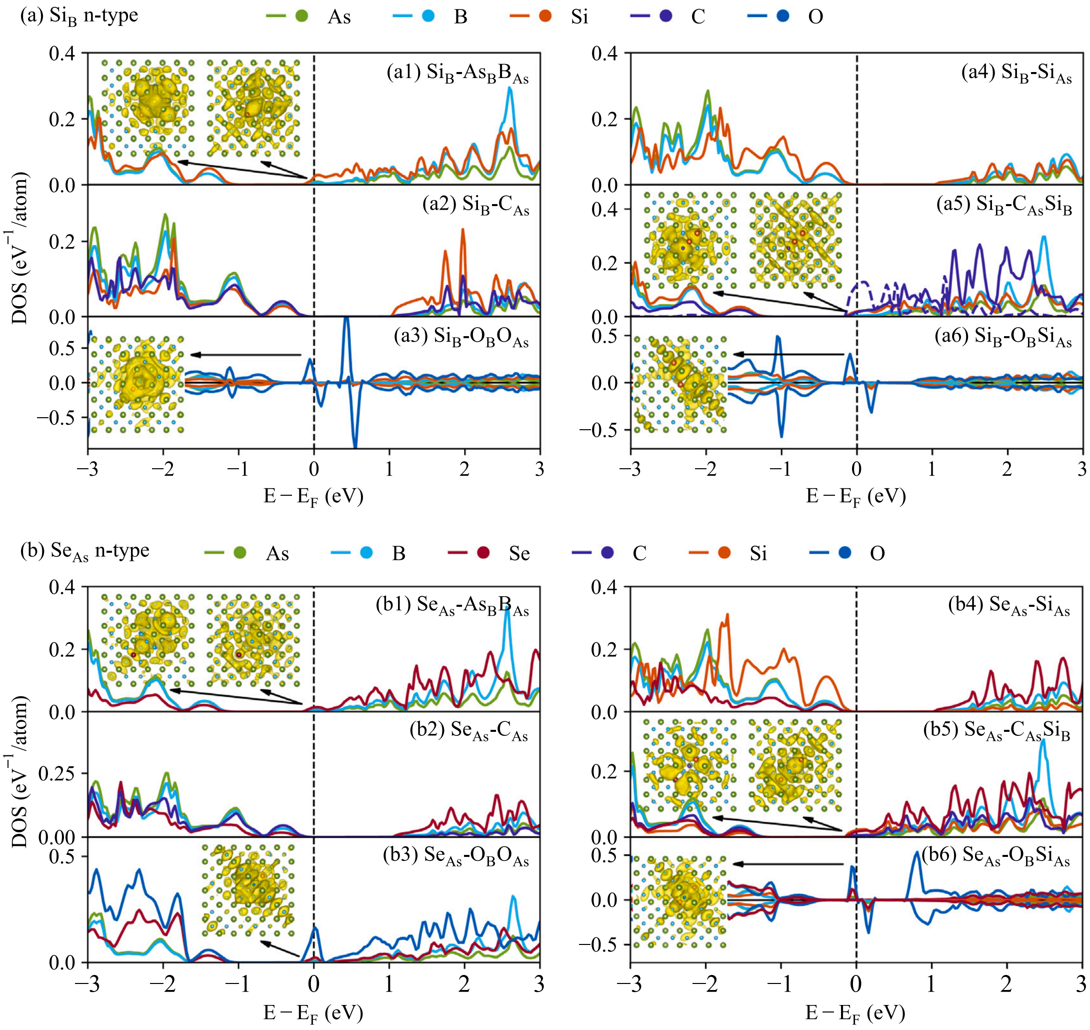

Fig. 5. Calculated electronic DOS of BAs doped by n-type dopants (a) Si_B and (b) Se_{As} in the presence of (1) As_BB_{As}, (2) C_{As}, (3) O_BO_{As}, (4) Si_{As}, (5) $C_{As}Si_B$, or (6) O_BSi_{As} point defects. The solid curves represent the DOS projection on *p* orbitals of each element, while the dashed curves represent the *s* orbital projection. The inset figures show the isosurfaces of charge density near CBM (<0.1 eV) or within the band gap, depicted at 4×10^{-5} Å^{-3}. The differently colored atoms represent different species.

line indicates that the coupled complex will likely form and preserve the shallow doping state.

Following these three scenarios, the O impurity proves detrimental to all four types of dopants by the results of O_BO_{As}. This necessitates restriction of O's concentration. Regarding C_{As} and Si_{As}, for p-type dopings Be_B and Si_{As}, concerns over C and Si impurities are alleviated; otherwise, for n-type dopings Si_B and Se_{As}, careful removal of C and Si impurities is imperative, which again emphasizes the lower n-type dopability in BAs. Most interestingly, the most favorable intrinsic defect, antisite defect pair As_BB_{As}, proves beneficial for all four types of dopants. Similar results can be confirmed for the other charge-neutral defect, $C_{As}Si_B$, which also is beneficial for three of the four types of dopants (excluding Si_B, where Si_B does not couple with $C_{As}Si_B$).

4. Conclusions

In conclusion, we have computed, from first principles, the formation energies and electronic characteristics of selected dopants, point defects, and coupled complexes of dopants and point defects in BAs. The shallow doping states of p-type dopants Be_B and Si_{As}, and n-type dopants Si_B and Se_{As}, were directly confirmed by the delocalized charge density isosurface near the Fermi level E_F. The favorable single point defects and point defect pairs for C, O, and Si impurities were identified (C_{As}, O_BO_{As}, Si_{As}, $C_{As}Si_B$, and O_BSi_{As}), all with formation energies of less than 1.5 eV. As for couplings between the selected dopants and defects, this study also identified the most favorable configurations. In terms of the influence of impurities on doping, the O impurity is detrimental to both p- and n-type doping, and C and Si impurities are detrimental to only n-type doping. Consequently, n-type doping is challenging, as it has a higher formation energy and requires the removal of C, Si, and O impurities. Interestingly, the most favorable intrinsic defect, antisite defect pair As_BB_{As}, positively impacts both the p- and n-type doping. These insights into the interactions between dopants and defects could potentially help expedite the further development of advanced electronics based on BAs, especially in understanding the doping limitation of n-type doping.

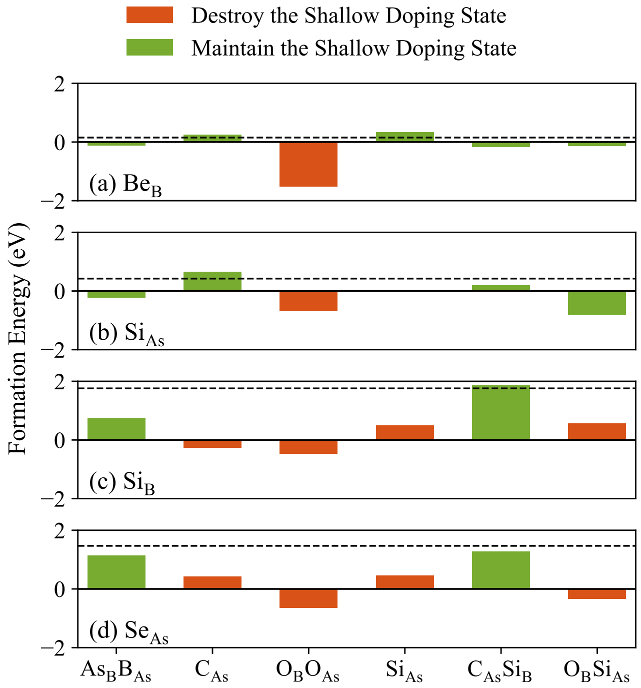

Fig. 6. Calculated formation energy of (a) Be_B, (b) Si_{As}, (c) Si_B, and (d) Se_{As} dopants in the presence of the selected point defects. The dashed lines represent the formation energy of dopants without defects. The colors of the bars indicate whether a detrimental influence of each point defect is observed on the shallow dopant.

CRediT authorship contribution statement

Shuxiang Zhou: Writing – original draft, Methodology, Investigation, Funding acquisition, Conceptualization. **Zilong Hua:** Writing – review & editing, Methodology, Conceptualization. **Kaustubh K. Bawane:** Writing – review & editing, Methodology, Conceptualization. **Hao Zhou:** Writing – review & editing, Methodology. **Tianli Feng:** Writing – review & editing, Methodology, Investigation, Funding acquisition, Conceptualization.

Declaration of competing interest

The authors declare that they have no known competing financial interests or personal relationships that could have appeared to influence the work reported in this paper.

Acknowledgments

This work is supported through the Idaho National Laboratory's Laboratory Directed Research and Development (LDRD) Program under DOE Idaho Operations Office Contract DE-AC07-05ID14517, LDRD Project ID 23A1070-064FP. This research made use of Idaho National Laboratory's High Performance Computing systems located at the Collaborative Computing Center and supported by the Office of Nuclear Energy of the U.S. Department of Energy and the Nuclear Science User Facilities under Contract No. DE-AC07-05ID14517.

Appendix A. Supplementary data

Supplementary material related to this article can be found online at https://doi.org/10.1016/j.commatsci.2024.113483.

Data availability

Data will be made available on request.

References

[1] D.A. Broido, L. Lindsay, T.L. Reinecke, Phys. Rev. B 88 (2013) 214303.
[2] L. Lindsay, D.A. Broido, T.L. Reinecke, Phys. Rev. Lett. 111 (2013) 025901.
[3] T. Feng, L. Lindsay, X. Ruan, Phys. Rev. B 96 (2017) 161201.
[4] J.S. Kang, M. Li, H. Wu, H. Nguyen, Y. Hu, Science 361 (2018) 575.
[5] F. Tian, B. Song, X. Chen, N.K. Ravichandran, Y. Lv, K. Chen, S. Sullivan, J. Kim, Y. Zhou, T.-H. Liu, M. Goni, Z. Ding, J. Sun, G.A.G. Udalamatta Gamage, H. Sun, H. Ziyaee, S. Huyan, L. Deng, J. Zhou, A.J. Schmidt, S. Chen, C.-W. Chu, P.Y. Huang, D. Broido, L. Shi, G. Chen, Z. Ren, Science 361 (2018) 582.
[6] S. Li, Q. Zheng, Y. Lv, X. Liu, X. Wang, P.Y. Huang, D.G. Cahill, B. Lv, Science 361 (2018) 579.
[7] T.-H. Liu, B. Song, L. Meroueh, Z. Ding, Q. Song, J. Zhou, M. Li, G. Chen, Phys. Rev. B 98 (2018) 081203.
[8] J. Shin, G.A. Gamage, Z. Ding, K. Chen, F. Tian, X. Qian, J. Zhou, H. Lee, J. Zhou, L. Shi, T. Nguyen, F. Han, M. Li, D. Broido, A. Schmidt, Z. Ren, G. Chen, Science 377 (2022) 437.
[9] S. Yue, F. Tian, X. Sui, M. Mohebinia, X. Wu, T. Tong, Z. Wang, B. Wu, Q. Zhang, Z. Ren, J. Bao, X. Liu, Science 377 (2022) 433.
[10] G.L.W. Hart, A. Zunger, Phys. Rev. B 62 (2000) 13522.
[11] R.M. Wentzcovitch, M.L. Cohen, J. Phys. C: Solid State Phys. 19 (1986) 6791.
[12] T. Joshi, P. Kumar, B. Poudyal, S.P. Russell, P. Manchanda, P. Dev, Phys. Rev. B 105 (2022) 054101.
[13] B. Lv, Y. Lan, X. Wang, Q. Zhang, Y. Hu, A.J. Jacobson, D. Broido, G. Chen, Z. Ren, C.-W. Chu, Appl. Phys. Lett. 106 (2015) 074105.
[14] J. Kim, D.A. Evans, D.P. Sellan, O.M. Williams, E. Ou, A.H. Cowley, L. Shi, Appl. Phys. Lett. 108 (2016) 201905.
[15] F. Tian, B. Song, B. Lv, J. Sun, S. Huyan, Q. Wu, J. Mao, Y. Ni, Z. Ding, S. Huberman, T.-H. Liu, G. Chen, S. Chen, C.-W. Chu, Z. Ren, Appl. Phys. Lett. 112 (2018) 031903.
[16] J. Xing, E.R. Glaser, B. Song, J.C. Culbertson, J.A. Freitas, Jr., R.A. Duncan, K.A. Nelson, G. Chen, N. Ni, Appl. Phys. Lett. 112 (2018) 241903.
[17] G.A. Gamage, H. Sun, H. Ziyaee, F. Tian, Z. Ren, Appl. Phys. Lett. 115 (2019) 092103.
[18] G.A. Gamage, K. Chen, G. Chen, F. Tian, Z. Ren, Mater. Today Phys. 11 (2019) 100160.
[19] B. Lv, Y. Lan, X. Wang, Q. Zhang, Y. Hu, A.J. Jacobson, D. Broido, G. Chen, Z. Ren, C.-W. Chu, Appl. Phys. Lett. 106 (2015) 074105.
[20] J. Xing, X. Chen, Y. Zhou, James. C. Culbertson, Jr. J.A. Freitas, E.R. Glaser, J. Zhou, L. Shi, N. Ni, Appl. Phys. Lett. 112 (2018) 261901.
[21] T.L. Chu, A.E. Hyslop, J. Appl. Phys. 43 (2003) 276.
[22] Q. Zheng, C.A. Polanco, M.-H. Du, L.R. Lindsay, M. Chi, J. Yan, B.C. Sales, Phys. Rev. Lett. 121 (2018) 105901.
[23] N.H. Protik, J. Carrete, N.A. Katcho, N. Mingo, D. Broido, Phys. Rev. B 94 (2016) 045207.
[24] M. Fava, N.H. Protik, C. Li, N.K. Ravichandran, J. Carrete, A. van Roekeghem, G.K.H. Madsen, N. Mingo, D. Broido, npj Comput. Mater. 7 (2021) 1.
[25] X. Chen, C. Li, Y. Xu, A. Dolocan, G. Seward, A. Van Roekeghem, F. Tian, J. Xing, S. Guo, N. Ni, Z. Ren, J. Zhou, N. Mingo, D. Broido, L. Shi, Chem. Mater. 33 (2021) 6974.
[26] J. Tang, G. Li, Q. Wang, J. Zheng, L. Cheng, R. Guo, Phys. Rev. Mater. 7 (2023) 044601.
[27] S. Chae, K. Mengle, J.T. Heron, E. Kioupakis, Appl. Phys. Lett. 113 (2018) 212101.
[28] J.L. Lyons, J.B. Varley, E.R. Glaser, J.A. Freitas, Jr., J.C. Culbertson, F. Tian, G.A. Gamage, H. Sun, H. Ziyaee, Z. Ren, Appl. Phys. Lett. 113 (2018) 251902.
[29] K. Bushick, K. Mengle, N. Sanders, E. Kioupakis, Appl. Phys. Lett. 114 (2019) 022101.
[30] X. Meng, A. Singh, R. Juneja, Y. Zhang, F. Tian, Z. Ren, A.K. Singh, L. Shi, J.-F. Lin, Y. Wang, Adv. Mater. 32 (2020) 2001942.
[31] Y. Wang, W. Windl, J. Appl. Phys. 129 (2021) 075703.
[32] P.E. Blöchl, Phys. Rev. B 50 (1994) 17953.
[33] G. Kresse, D. Joubert, Phys. Rev. B 59 (1999) 1758.
[34] G. Kresse, J. Hafner, Phys. Rev. B 47 (1993) 558.
[35] G. Kresse, J. Furthmüller, Phys. Rev. B 54 (1996) 11169.
[36] J.P. Perdew, A. Ruzsinszky, G.I. Csonka, O.A. Vydrov, G.E. Scuseria, L.A. Constantin, X. Zhou, K. Burke, Phys. Rev. Lett. 100 (2008) 136406.
[37] A. Droghetti, C.D. Pemmaraju, S. Sanvito, Phys. Rev. B 78 (2008) 140404, publisher: American Physical Society.
[38] K. Momma, F. Izumi, J. Appl. Crystallogr. 44 (2011) 1272.
[39] F.A. Kröger, H.J. Vink, in: F. Seitz, D. Turnbull (Eds.), Solid State Physics, vol. 3, Academic Press, 1956, pp. 307–435.